Table 3. Material parameters of combined energy model in representing elongation, compression and combined compression and then elongation experimental data.

$$W = \frac{C_1}{2}\ln(1 - C_2(I_1 - 3)) + C_3(I_1 - 3)$$

	Elongation	Compression	Combined Compression and Elongation
C_1	−337.7	−7881.1	−342.4
C_2	2.2	1.6	1.9
C_3	−287.7	−3941.4	−136.0

representation and negative in another. This pitfall was typical with polynomial-based constitutive equation. It could cause very different mechanical behavior in 3D cases and pose serious accuracy issues during numerical analysis such as finite element method.[48] Table 3 lists the material constants used in the combined energy model to fit the average stress–strain curve respectively from elongation, compression and combined compression and elongation experiments. More details on the curve fitting results can be found in Chui *et al.*[25]

We repeated the analyses for liver tissue with porcine kidney and brain tissues. The experimental conditions and procedures were the same for all three types of soft tissues. A close fit was possible with the combined logarithmic and polynomial model. The combined logarithmic and polynomial model could model these tissues with similar errors, and small deviations in material parameters. The polarity of the parameters did not change in the combined model. This demonstrates the suitability of our combined logarithmic and polynomial energy function as the model of choice for soft tissues in general and liver tissue in particular. The experiments with porcine kidney and brain tissues were conducted preliminary with five test samples each.

5.3. *Image based inverse finite element parameter estimation*

Although the strain energy based constitutive equations are generally valid for three-dimensional stress state, the material parameters determined in this section are limited by the uniaxial loading experiments. Typical multi-axial experiments involve frozen tissue. This will inevitably alter the biomechanics of underlying tissue. Image based inverse finite element parameter estimation could be used in conjunction with uniaxial combined compression and elongation experiments to determine the material parameters of liver tissue in three-dimensional stress state.

Figure 13(a) is a flow chart that illustrates the process. Input to the method was video images of the deformation. The video was processed and separated into individual frames of deformation with known force and time. A displacement driven axisymmetric finite element model of the tissue sample was developed to determine mechanical properties of liver tissue (Figure 13(b)). This generic model was adjusted to represent liver tissue sample height measured during experiments. The diameter

of the sample was set at 7 mm. The planar surface was assumed to be flat and bonded to the hard rubber plates. Due to asymmetry, only 1/8 of the tissue sample is required to be modelled. The model comprises of eight nodes brick elements. MARC 7 a commercially available finite element solver is used in conjunction with Patran 2001 (MSC Software Corporation, USA), a pre- and post processor for CAE simulation, in the solution process as well as material properties assignment. From the list of instantaneous parameters, a set of parameters is selected based on its ability to model the stress–strain curve.

Recall that Piola-Kirchhoff stress can be expressed in terms of energy W and Green–Lagrange strain E_{ij} as follows:

$$S_{ij} = \frac{\partial(W)}{\partial E_{ij}}.$$

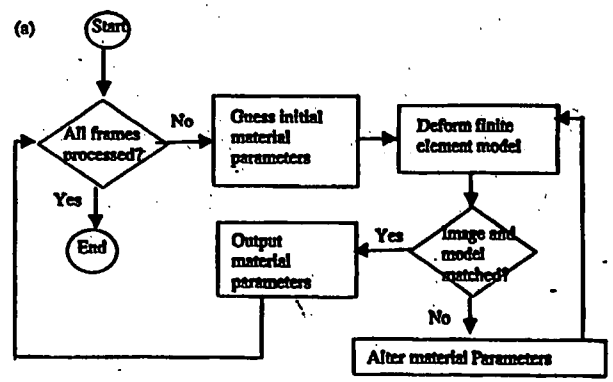

Fig. 13(a). Overview of image based inverse finite element parameters estimation: flow chart for estimation of material parameters for instantaneous deformation.

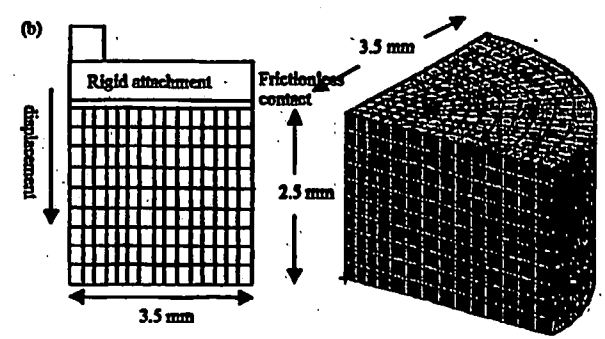

Fig. 13(b). Overview of image based inverse finite element parameters estimation: finite element modeling.

For modeling of biological soft tissue, a popular constitutive equation was the pseudo-strain-energy function proposed by Fung.[52] Following is the original generalized exponential equation where α_{ijk}, β_0, β_{mnpq}, γ_{ij} and κ_{ijkl} are constants to be determined empirically,

$$W = \frac{1}{2}\alpha_{ijk}E_{ij}E_{kl} + (\beta_0 + \beta_{mnpq}E_{mn}E_{pq})\exp(\nu_{ij}E_{ij} + \kappa_{ijk}E_{ij}E_{kl} + \cdots).$$

The derivation could be illustrated by first considering a two dimension problem space. Following equation is the simplified 2D version that is valid for the physiological range. Note that $E_{12}$is the shear.

$$\begin{aligned} W = {} & \frac{1}{2}(\alpha_1 E_{11}^2 + \alpha_2 E_{22}^2 + \alpha_3 E_{12}^2 + \alpha_3 E_{21}^2 + 2\alpha_4 E_{11}E_{22}) \\ & + \frac{1}{2}C\exp(a_1 E_{11}^2 + a_2 E_{22}^2 + a_3 E_{12}^2 + a_3 E_{21}^2 + 2a_4 E_{11}E_{22} \\ & + \nu_1 E_{11}^3 + \nu_2 E_{22}^3 + \nu_4 E_{11}^2 E_{22} + \nu_5 E_{11}E_{11}^2). \end{aligned}$$

By having ν's terms equal to 0, the equation can be simplified further to

$$W = f(\alpha, E) + C\exp(F(a, E)),$$

where

$$\begin{aligned} f(\alpha, E) &= \alpha_1 E_{11}^2 + \alpha_2 E_{22}^2 + \alpha_3 E_{12}^2 + \alpha_3 E_{21}^2 + 2\alpha_4 E_{11}E_{22}, \\ F(a, E) &= a_1 E_{11}^2 + a_2 E_{22}^2 + a_3 E_{12}^2 + a_3 E_{21}^2 + 2a_4 E_{11}E_{22}. \end{aligned}$$

If we are considering physiological range only and have no concern on very small strain, we can simplify the exponential energy function further to

$$W = C\exp(F(a, E)).$$

Assuming that liver tissue is isotropic ($E_{12} = E_{21}$),

$$F(a, E) = a_1(E_{11}^2 + E_{22}^2) + 2a_3 E_{12}^2 + 2a_4 E_{11}E_{22}.$$

Following is the corresponding exponential term in a 3D problem space. The assumption on material isotropy implies that $E_{12} = E_{21}$, $E_{23} = E_{32}$ and $E_{13} = E_{31}$. Also $a_1 = a_2 = a_3$, $a_4 = a_5 = a_6$ and $a_7 = a_8 = a_9$. This leads to

$$\begin{aligned} F(a, E) &= a_1 E_{11}^2 + a_2 E_{22}^2 + a_3 E_{33}^2 + a_4 E_{12}^2 + a_4 E_{21}^2 \\ &\quad + a_5 E_{23}^2 + a_5 E_{32}^2 + a_6 E_{13}^2 + a_6 E_{31}^2 \\ &\quad + 2a_7 E_{11}E_{22} + 2a_8 E_{22}E_{33} + 2a_9 E_{33}E_{11} \\ &= a_1(E_{11}^2 + E_{22}^2 + E_{33}^2) + 2a_4(E_{12}^2 + E_{23}^2 + E_{31}^2) \\ &\quad + 2a_7(E_{11}E_{12} + E_{22}E_{23} + E_{33}E_{31}). \end{aligned}$$

Hence,

$$W = C\exp(F(a, E)),$$

where

$$\begin{aligned} F(a, E) = {} & a_1(E_{11}^2 + E_{22}^2 + E_{33}^2) + 2a_4(E_{12}^2 + E_{23}^2 + E_{31}^2) \\ & + 2a_7(E_{11}E_{12} + E_{22}E_{23} + E_{33}E_{31}) \end{aligned}$$

Note that if effect from shear is not considered then $a_4 = a_5 = a_6 = 0$. If the effect similar to Poisson's ratio is negligible, $a_7 = a_8 = a_9 = 0$.

Equivalent logarithmic energy function is given as follows:

$$W = -C\ln(F(a, E)),$$

where

$$\begin{aligned} F(a, E) = {} & \frac{a_1}{2}(E_{11}^2 + E_{22}^2 + E_{33}^2) + a_4(E_{12}^2 + E_{23}^2 + E_{31}^2) \\ & + a_7(E_{11}E_{12} + E_{22}E_{23} + E_{33}E_{31}). \end{aligned}$$

The corresponding combined logarithmic and polynomial energy function is as follows:

$$W = -\frac{C}{2}\ln(1 - F(a, E)) - \frac{C}{2}F(a, E) + \frac{F_1(a, E)}{2},$$

where

$$\begin{aligned} F(a, E) = {} & \frac{a_1}{2}(E_{11}^2 + E_{22}^2 + E_{33}^2) + a_4(E_{12}^2 + E_{23}^2 + E_{31}^2) \\ & + a_7(E_{11}E_{12} + E_{22}E_{23} + E_{33}E_{31}) \\ F_1(a, E) = {} & \frac{a_{10}}{2}(E_{11}^2 + E_{22}^2 + E_{33}^2) + a_{11}(E_{12}^2 + E_{23}^2 + E_{31}^2) \\ & + a_{12}(E_{11}E_{12} + E_{22}E_{23} + E_{33}E_{31}). \end{aligned}$$

In modeling the uniaxial tension/compression tests that we performed, the shear terms are ignored. The exponential strain energy functions in 2D problem spaces become

$$W = C\exp(F(a, E)),$$

where

$$F(a, E) = a_1(E_{11}^2 + E_{22}^2) + 2a_4 E_{11}E_{22}.$$

The corresponding equation in 3D is

$$W = C\exp(F(a, E)),$$

where

$$F(a,E) = a_1(E_{11}^2 + E_{22}^2 + E_{33}^2) + 2a_7(E_{11}E_{12} + E_{22}E_{23} + E_{33}E_{31}).$$

The equivalent logarithmic energy functions in 2D and 3D problem spaces are respectively,

$$W = -C\ln(F(a,E)),$$

where

$$F(a,E) = \frac{a_1}{2}(E_{11}^2 + E_{22}^2) + a_4E_{11}E_{22}$$

and

$$W = -C\ln(F(a,E)),$$

where

$$F(a,E) = \frac{a_1}{2}(E_{11}^2 + E_{22}^2 + E_{33}^2) + a_7(E_{11}E_{12} + E_{22}E_{23} + E_{33}E_{31}).$$

The combined logarithmic and polynomial energy function for non isotropic material in 3D space is

$$W = -\frac{C}{2}\ln(1 - F(a,E)) - \frac{C}{2}F(a,E) + \frac{F_1(a,E)}{2},$$

where

$$F(a,E) = \frac{a_1}{2}(E_{11}^2 + E_{22}^2 + E_{33}^2) + a_7(E_{11}E_{12} + E_{22}E_{23} + E_{33}E_{31}),$$

$$F_1(a,E) = \frac{a_{10}}{2}(E_{11}^2 + E_{22}^2 + E_{33}^2) + a_{12}(E_{11}E_{12} + E_{22}E_{23} + E_{33}E_{31}).$$

The inverse approach to determine liver material properties involve comparing the experimental data with theoretical stress and strain calculated using finite element method. The liver material properties are expressed in terms of material constants in various energy functions.

Figure 14(a) illustrates the comparison of images of experiments and finite element deformation of the liver tissue sample at six regular intervals. It is possible to obtain a good fit with the stress–strain curve from elongation test using appropriate material parameters as shown in Fig. 14(b).

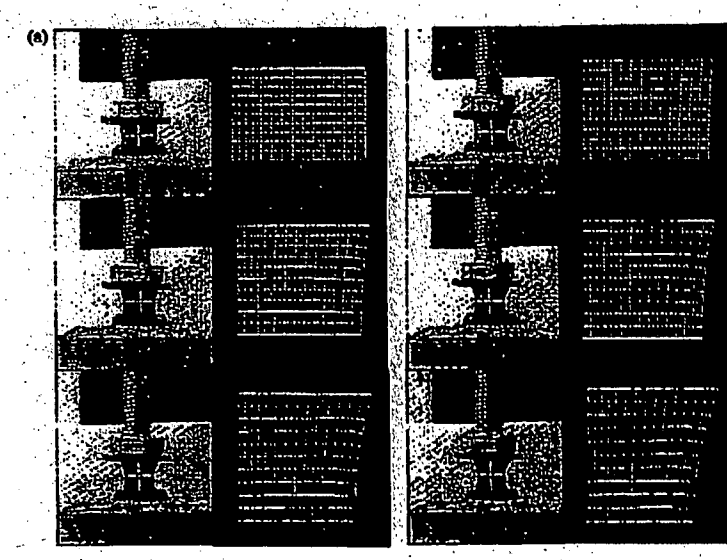

Fig. 14(a). Results from inverse finite element parameters estimation: matching of deformed model and images of experiment.

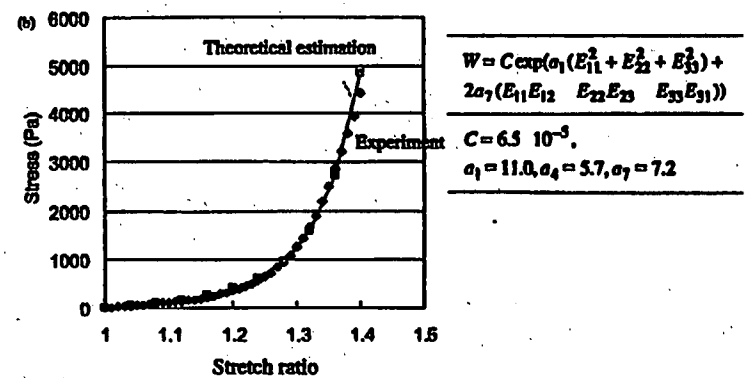

Fig. 14(b). Results from inverse finite element parameters estimation: curve fitting of experimental stress–strain curve.

5.4. *Multi-linear constitutive equation*

Fast computation with reasonable accuracy is desired in computer aided surgical simulation. A multi-linear constitutive equation defined on the concept of equivalent stress may be appropriate for such applications. The constitutive model assumes that the mechanical properties of liver tissue are isotropic and could be defined using instantiated elastic modulus and Poisson's ratio from stress–strain curve.

We refer to a cylindrical sample of liver tissue undergoing uniaxial tension and/or compression test. If the slope of σ versus ϵ is plotted against σ, the result was a roughly straight curve. We may fit this experimental curve by a series of straight lines, i.e.

$$\frac{d\sigma}{d\varepsilon} = \alpha_1(\sigma + \beta_1), \quad 0 \le \sigma \le \sigma_1$$
$$\frac{d\sigma}{d\varepsilon} = \alpha_2(\sigma + \beta_1), \quad \sigma_1 \le \sigma \le \sigma_2$$

An integration gives

$$\sigma + \beta_1 = c_1 \exp(\alpha_1 \varepsilon), \quad 0 \le \sigma \le \sigma_1$$
$$\sigma + \beta_2 = c_2 \exp(\alpha_2 \varepsilon), \quad \sigma_1 \le \sigma \le \sigma_2$$

and

$$\sigma = c_1 \exp(\alpha_1 \varepsilon) - \beta_1, \quad 0 \le \sigma \le \sigma_1$$
$$\sigma = c_2 \exp(\alpha_2 \varepsilon) - \beta_2, \quad \sigma_1 \le \sigma \le \sigma_2 \tag{4}$$

The integration constants can be determined by curve fitting this equation with the original experimental stress–strain curve. Stress is used to define the intervals. Strain can also be used by simply start with a curve with slope of σ versus ϵ is plotted against ε.

Representation of the stress–strain curve can also be done via piece-wise approximation using linear functions treating each line segment as a linear elastic material. Following is the bilinear constitutive model:

$$\sigma = E_0 \varepsilon_0, \quad \varepsilon \le \varepsilon^*$$
$$\sigma = E(\varepsilon - \varepsilon^*) + E_0 \varepsilon^*, \quad \varepsilon > \varepsilon^*,$$

where E_0 is Young's modulus at the toe region, ε^* is the strain at toe-linear region. An issue with this model is that it is very sensitive to the definition of the maximum stress. The following multi-linear constitutive model is proposed to represent the nonlinear material model.

$$\sigma = E_0 \varepsilon_0, \quad \varepsilon \le \varepsilon^*$$
$$\sigma = E_i \left(\varepsilon_i - \sum_{j=0}^{i-1} \varepsilon_j \right) + \sum_{j=0}^{i-1} E_j \varepsilon_j, \quad \varepsilon > \varepsilon_i^*,$$

To define the intervals ε_i, curve fitting was applied on the $d\varepsilon - \sigma$ curve with Eq. (4). A region/interval was established when the residual error from the fitting

was greater than a tolerance. In this study, a very small tolerance of 0.00001 was used.

$$\sigma = C_1(\varepsilon + C_2) = C_1\varepsilon + C_3$$

where C_1, C_2 and $C_3 = C_1C_2$ are constants, and $d\varepsilon$ is the Young's modulus. Hence, the relation at each interval is expressed in terms of straight lines. The parameter C_1 represents the rate of increase of the elastic modulus with respect to increasing tension or compression corresponding to the slope of the curve. The parameter C_3 is the intercept of the straight-line segment extended to zero stress.

Note that unloading at the same strain rate results in similar straight lines with different slopes. In view of the significant difference during loading and unloading of liver tissue, loading and unloading should be in fact considered as two different materials. Only loading curve is considered. The multi-linear constitutive model is a more direct approach compared to the exponential based method and is the focus of this section. Multi-linear constitutive model is also applicable to Poisson's ratio. However, the Poisson's ratio of liver tissue was found to vary around 0.5, and considering the infusion of blood in patient's liver organ, we assume that liver tissue is incompressible.

5.4.1. *Equivalent stress and strain for multi-axial state*

The constitutive equations described above are often good practical choices for fast surgical simulation with less emphasis on accuracy. They do not reduce to the form of strain energy and generally are not valid for three dimensional stress states. To relate the uniaxial stress–strain relationship represented by these constitutive equations with the general multi-axial stress–strain relationship, equivalent stress and strain is proposed as the "bridge" for this correlation.

The engineering stress T is the load F divided by the cross-sectional area of the specimen at zero stress state, A_0. The engineering strain e is defined as the ratio between displacement $(L_f - L_0)$ and the original length of the specimen L_0. T and e were measured in our experiments. As was described earlier, liver tissue being a nonlinear material, true or nature stress σ and strain ε should be used since we seek to model large strain deformation. The following definitions for true stress and strain are used.

$$\varepsilon = \int_0^{\varepsilon} dE = \int_{L_0}^{L_f} \frac{dL}{L} = \ln \frac{L_d}{L_0} \tag{5}$$

where dL is the incremental change and L is the length at beginning of increment.

$$\sigma = \frac{F}{A}$$

where A is the instantaneous cross sectional area of the deformed specimen. From Eq. (5) and definition of engineering strain, we arrived at the following relationship between engineering and true strain,

$$\varepsilon = \ln(1+e). \tag{6}$$

Similarly, the following relationship between engineering and true stress can be established,

$$\sigma = T(1+e).$$

After determining the true stress and stress from uniaxial experiment, it is necessary to relate this uniaxial observation to stress and strain in the general state. For this purpose, we assume that for any given stress state, there exists an equivalent uniaxial stress state generally associated with plastic deformation.[51] For realistic simulation of 3D deformation, it is suffice to define six stress components $(\sigma_x, \sigma_y, \sigma_z, \tau_{xy}, \tau_{yz}, \tau_{zx})$ and six strain components $(\varepsilon_x, \varepsilon_y, \varepsilon_z, \nu_{xy}, \nu_{yz}, \nu_{zx})$ under multi-axial stress-strain state. The equivalent stress σ_e, also known as von Mises stress and equivalent strain ε_e are defined as follows

$$\sigma_e = \frac{1}{\sqrt{2}}((\sigma_x-\sigma_y)^2+(\sigma_y-\sigma_z)^2+(\sigma_z-\sigma_x)^2+6(\tau_{xy}^2+\tau_{yz}^2+\tau_{zx}^2)).$$

$$\varepsilon = \int d\varepsilon_e,$$

where $d\varepsilon_e$ is the strain increment defined as follows

$$d\varepsilon_e = \frac{\sqrt{2}}{3}((d\varepsilon_x-d\varepsilon_y)^2+(d\varepsilon_y-d\varepsilon_z)^2+(d\varepsilon_z-d\varepsilon_x)^2+6(d\nu_{xy}^2+d\nu_{yz}^2+d\nu_{zx}^2)).$$

During finite element simulation with multi-axial state of stress, the computed stress of the finite element will be first converted to the equivalent stress. This is to select the appropriate region in the multi-linear constitutive model for representation of the material properties of the soft tissue at the finite element. Under uniaxial state of stress,

$$\sigma_z = \sigma$$
$$\sigma_x = \sigma_y = \tau_{xy} = \tau_{yz} = \tau_{zx} = 0.$$

We assume that liver is isotropic and incompressible. Hence,

$$\varepsilon_z = \varepsilon$$
$$\varepsilon_x = \varepsilon_y = -\frac{\varepsilon}{2}$$
$$\nu_{xy} = \nu_{yz} = \nu_{zx} = 0.$$

Since $\sigma_e = \sigma_z = \sigma$ and similarly for strain, followed by integration by parts,

$$\varepsilon_e = \int d\varepsilon = \varepsilon.$$

Hence, it is suffice for us to assume that the equivalent stress is the true stress and equivalent strain is the true strain under uniaxial state of stress and strain.

Figure 15 illustrated the variation of elastic modulus calculated from average true stress and strain curves with true stress during compression and elongation test. The variation in elongation was relatively smaller and could be represented using several straight lines. Nevertheless, in the case of compression, we observed much disparity in the fitting the experiment data with straight lines. More straight lines were required to fit this experimental data. The variations defined the intervals where elastic modulus is desired.

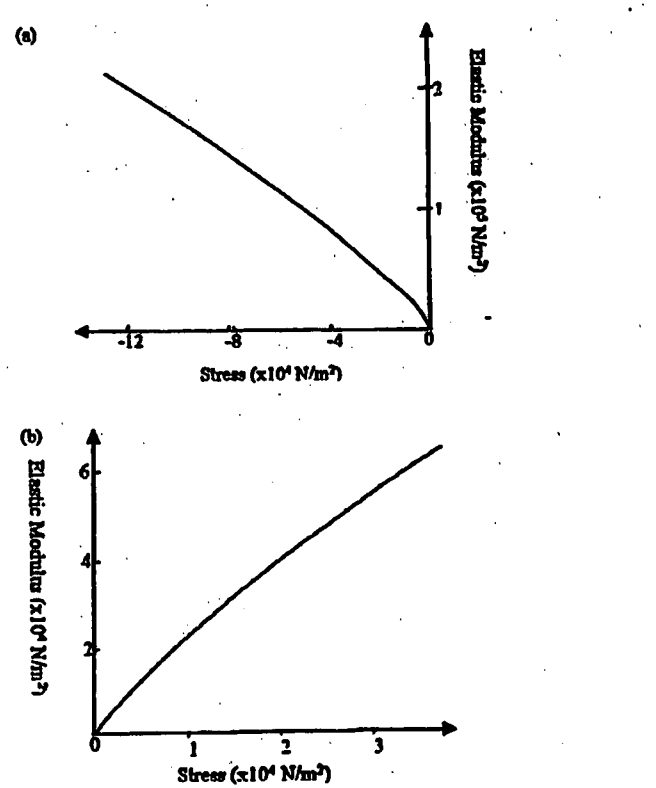

Fig. 15. Variation of elastic modulus with stress for (a) elongation and (b) compression. The stress for elongation and compression was an average of the data listed in Table 1 and Table 2 respectively.

Table 4. Material parameters of equivalent stress and strain based multi-linear constitutive model.

$$\sigma = E_0\varepsilon_0, \quad \varepsilon \le \varepsilon_0$$
$$\sigma = E_i\left(\varepsilon_i - \sum_{j=0}^{i-1}\varepsilon_j\right) + \sum_{j=0}^{i-1}E_j\varepsilon_j, \quad \varepsilon > \varepsilon_i$$

Strain Intervals, ε_i	Elastic Modulus, $E_i(\times 10^4\,N/m^2)$	Stress Intervals $(\times 10^4\,N/m^2)$
−0.57 to −0.60	−424.133	−11.067 to −12.724
−0.55 to −0.57	−553.350	−9.180 to −11.067
−0.52 to −0.55	−305.999	−6.348 to −9.180
−0.48 to −0.52	−158.699	−4.887 to −6.348
−0.46 to −0.48	−244.380	−3.404 to −4.887
−0.42 to −0.46	−85.112	−2.101 to −3.404
−0.36 to −0.42	−35.018	−0.887 to −2.101
0.00 to −0.36	−2.465	0.00 to −0.887
0.00 to 0.38	1.176	0.00 to 0.447
0.38 to 0.43	17.600	0.447 to 0.880
0.43 to 0.48	34.740	0.880 to 1.737
0.48 to 0.52	63.699	1.737 to 2.548
0.52 to 0.54	148.154	2.548 to 2.963
0.54 to 0.58	95.502	2.963 to 3.820

6. Finite Element Simulation of Soft Tissue Deformation

Accuracy and computational time are two main constraints in the practical application of soft tissue modeling. Depending on the applications, there are different requirements in these two criteria. Typically, simulation for surgical planning may have from 30 s to 1 h to deliver a clinically relevant result for outcome prediction. A surgical procedure training system will have computational time in the order of 0.1 s to achieve smooth user interaction whereas accuracy of deformation is not necessary of primary important. There were interactive computer simulations based on techniques in biomechanical engineering and computer graphics, e.g.[55]

An approach in simulation of soft tissue deformation is via finite element method. Finite element based simulation of soft tissue deformation have been applied both in surgical simulators[6,56,57] as well as elastic image registration.[58,59] The multi-linear constitutive equation is an appropriate material model for surgical training application that demands fast computation with reasonable accuracy. The strain energy based constitutive equations should be used when higher accuracy is desired.

The main motivation of employing von Mises stress in multi-linear constitutive model is its ability to predict nonlinear stress–strain relationship at and after yield point. In order to validate the hypothesis of our scheme in relating the multi-axial stress and strain with that measured during uniaxial experiments, independent experiments were conducted, and the recorded experimental deformation were

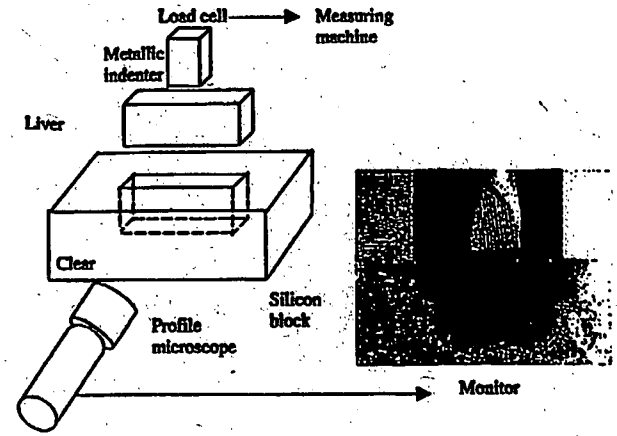

Fig. 16. *In vitro* experiment with multi-axial deformation. Tissue of rectangular shape was extracted from porcine liver organ and placed inside a hole of the same size in a silicon block. The deformation of the liver tissue was recorded using a profile microscope. Insert is snap shot of experimental tissue sample at zero stress state.

compared with that of the corresponding finite element simulation using the multi-linear constitutive equation described above. The experimental setup (Fig. 16) was similar to that of our uniaxial experiment described earlier. A rectangular block of porcine liver tissue sample with dimension 30 mm × 10 mm × 10 mm was used in an indentation test. The test resembles the multi-axial structure problem involving local load on half space. A uniform load from an indenter with a square base (10 mm × 10mm) was applied on the top surface of the sample. The sample was placed in a transparent silicon block with dimension 30 mm × 10 mm × 10 mm. Recording of the deformation was done using a profile microscope. The loading rate and other conditions were the same as that of the compression and elongation tests at 10 mm/min.

Figure 17 shows finite element simulation of the rectangular block sample, and corresponding deformation on the X–Y plane recorded at various time steps. In this simulation, we use MARC 7 for finite element analysis and Patran 2001 as pre- and post processor. There were a total of 657 TETRA4 elements and 208 nodes in the model. The material was represented using the multi-linear constitutive model. Boundary conditions are imposed at the bottom and the four sides. Since the deformation is relatively large at 1 mm, 2 mm and 3 mm, geometrical nonlinear condition was imposed and hence, a nonlinear solver was used in the solution process. The simulated deformations were compared with the recorded images during the experiment. It was observed that the deformation from finite element simulation consistently smaller than that of the recorded images by an almost

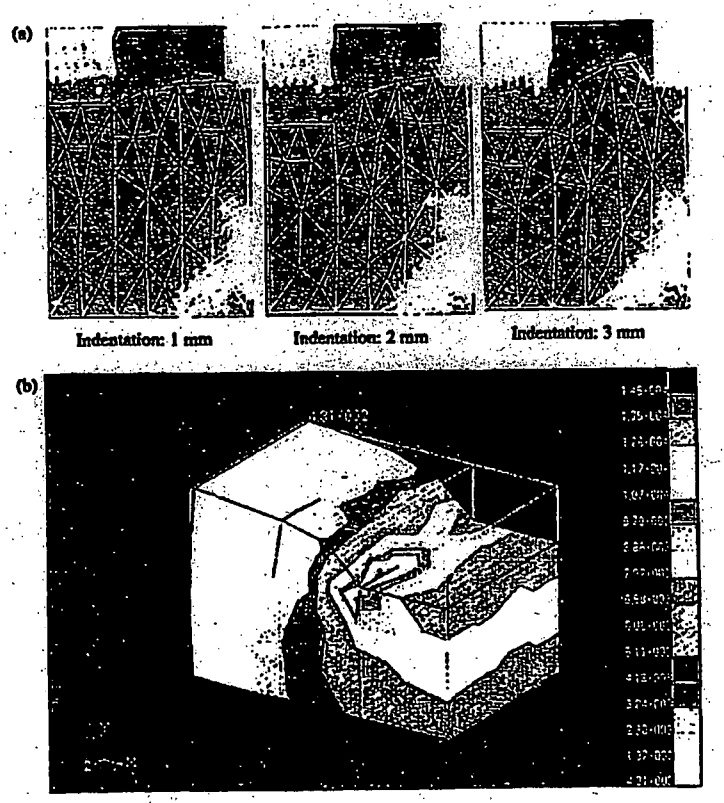

Fig. 17. Finite element simulation of multi-axial deformation experiment. (a) The simulated deformation (drawn with mesh lines) is compared with the recorded deformation at various instants. (b) Equivalent stress distribution at 3 mm indentation.

constant area. This inconsistency was possibly due to the imperfect condition of the experiments. For example, friction was not considered in the computational study. Although precaution have been taken to avoid the liver tissue becoming dry, friction was inevitable. Nevertheless, this shortfall is rather consistent. The simulation is reasonably accurate if this offset is considered.

To quantitatively evaluate the "match" between the computational and experimental deformation, we use the root-mean-square value of the residual as the quantitative standard error indicator for the match. Residual can be defined as the difference between the observed and predicted data. Suppose that A is the residual of deformed contors predicted by the computational method and experimental method. The root-mean-square value is equal to $\text{norm}(A)/\sqrt{n}$ where n is the number of

elements in A, and $\text{norm}(A) = \sqrt{\sum A^2}$. The standard error for the deformation at deformation 1 mm, 2 mm and 3 mm are: in x direction — 0.48 mm, 1.15 mm and 2.02 mm; in y direction — 0.63 mm, 1.11 mm and 0.22 mm. The average percentage of error is 8% and 4 % respectively. The relatively small error prompted us to believe that the computational deformation will match the corresponding experimental deformation if the rather consistent shortfall described in previous paragraph has been taken care off. Hence, the validity of using equivalent stress and strain as the "bridge" to transform the uniaxial experiment and constitutive model to the general multi-axial state was demonstrated.

The strain is generally greater than 10% during surgical simulation. This is large deformation by definition. Numerically, static finite element method, also known as small strain theory, does not apply here. In this case, finite element method based on finite deformation should be used. In the previous paragraph, the nonlinear solver takes an average CPU time of 0.1 s for a 17 steps deformation analysis on an Intel Pentium III 1.2 GHz notebook computer. This is equivalent to about 10 frames per second. Figure 18(a) is a high resolution finite element model of human liver organ. Figure 18(b) shows the corresponding low resolution finite element model deformed under force applied from the front with a large probe. The deformation is near real time with approximately 12 frames per second using a customized nonlinear finite element code. It might be possible to achieve real time interaction for the high resolution model if deformation can be considered local and small strain theory is applicable.

The requirement of fast computation prompted many investigators to exploit the possible use of small strain theory in medical simulation. For application of small strain theory, we can divide the large deformation into a number of much smaller displacement steps. For each small displacement step, the strain components are computed using Cauchy's infinitesimal strain tensor formula. Note that in this case, the incremental errors introduced by small strain formulation were assumed to be

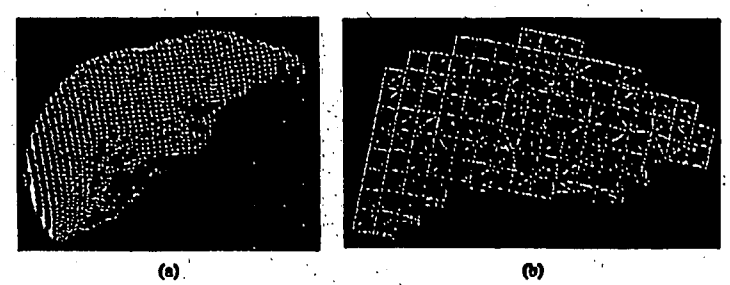

Fig. 18. Finite element modeling and simulation of human liver organ. (a) High resolution finite element model; (b) deformation of low resolution finite element model of liver with 3470 linear tetrahedral elements and 1079 nodes.

small and can be neglected

$$\varepsilon_x = \frac{\partial u}{\partial x}, \quad \varepsilon_y = \frac{\partial v}{\partial y}, \quad \varepsilon_z = \frac{\partial w}{\partial z}$$

$$\nu_{xy} = \frac{1}{2}\left(\frac{\partial u}{\partial y} + \frac{\partial v}{\partial x}\right), \quad \nu_{yz} = \frac{1}{2}\left(\frac{\partial v}{\partial z} + \frac{\partial w}{\partial y}\right), \quad \nu_{zx} = \frac{1}{2}\left(\frac{\partial u}{\partial z} + \frac{\partial w}{\partial x}\right),$$

where $u = u(x, y, z)$, $v = v(x, y, z)$ and $w = w(x, y, z)$ are the displacement fields in the x, y and z directions respectively, from one small displacement iteration to another. Nodal stress in the finite element is then computed using conventional linear finite element method.

Figure 19 illustrates a 2D deformation of the liver due to needle insertion using the small strain theory and the multi-linear constitute model. A frictionless contact was assumed. We also assume that a node fails when the stress at the node is greater

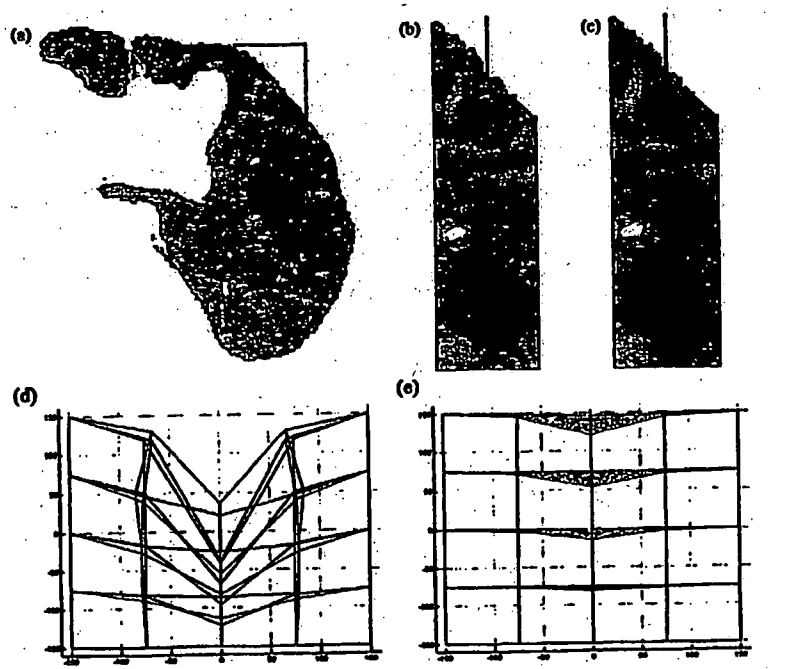

Fig. 19. Finite element simulation of liver deformation due to needle insertion: (a) planar view of a human liver with a synthesized tumor; (b) deformation of liver surface due to insertion of needle; (c) deformation and subsequent cutting of liver tissue during needle insertion; (d) view of the deformation sequence using multi-linear model; (e) view of the deformation sequence using linear elastic model.

than the break stress of liver during compression (2.313×10^5 Pa). In Fig. 19(b), the liver surface was first deformed by the introduction of a needle. The deformation of the liver continues until the maximum stress of the liver tissue reached in Fig. 19(c). Figures 19(d) and 19(e) compares the deformation sequence from the multi-linear model and that of the linear elastic model a constant Young's modulus at 625 kPa (see Sec. 4). The former agrees with the nonlinear force–displacement behavior of liver tissue during deformation and is clearly closer to the deformation observed during surgery.

7. Concluding Remarks

An experimental approach can be adopted in the study of biomechanical modeling for computer aided surgical simulation. The approach involves deriving the theoretical models based on experimental results from customary designed experiments, and validating surgical simulation that are based on these models using experiments. The focus of this study is on liver organ.

Understanding the biomechanics of liver is important in virtual reality based surgical simulation as well as actual surgical intervention and medical image registration.[59–61] Various methods on measuring and modeling of tissue for computer aided surgery have been reported in the literature. These include simple poking interaction using biological or phantom tissue, e.g.[62,63] viscoelastic characterization of tissue, e.g.[64] as well as uniaxial loading and indentation experiments with porcine liver.[19,20,25,26] To validate the biomechanical model, Howe and colleagues developed a phantom known as "Truth Cube".[65] However, the truth cube does not consider tissue probing and cutting which are among the most common surgical tasks. Recent study[66] has attempted to compare human and porcine kidney tissues. It is generally believe that the mechanical properties of human and porcine liver tissues are similar.

Validation of computer aided surgical application is itself a challenging problem. In order to have adequate validation of, e.g. needle insertion, we need to track the needle path possibly using some imaging modalities, among the many practical issues to be considered. Although we are confident of the clinical viability of the biomechanical model and simulation, there remain some challenging research issues that warrant further investigation.

7.1. *Methods of experiment*

There are limitations with the uniaxial elongation or compression experiments in this study. The alternative multi-axial tests will subject the tissue sample to tremor such as extensive cutting and possibly freezing. We have conducted independent experiments and found that freezing will cause significant changes to the mechanical properties of liver tissue. Hence, we are of the view that uniaxial test is a feasible and preferred

approach in this context. Given that the standard deviation of the experimental stress–strain data was high, it is important to improve the accuracy of subsequent numeric computations in analysis. A possible statistical method is normalization which is a process of scaling the numbers in a data set. A way to normalize the stress–strain data is to center the strain data at zero mean and scale it to unit standard deviation. The "goodness" of fit could be improved with the normalized stress–strain curve. The standard errors in curve fitting should be smaller.

To relate the general multi-axial state in 3D deformation with the stress–strain relation from uniaxial test, the concept of equivalent stress and strain could be used as the intermediate layer. The mechanical properties of liver tissue can possibly be defined upon the lower level liver lobules. The work on measuring and modeling the mechanical properties of liver lobules is on going. Relating tissue at macro and micro scales were previously investigated by Vawter *et al.*[67] for lung.

An interesting topic for our future pursuit in experimental biomechanics is to measure the mechanical properties of liver cells and investigate their relationship with the liver lobule and the liver tissue. Preparation of the liver cell sample and the associated engineering issues such as micromanipulator control are problems that we have faced in our attempted investigation beyond liver lobule.

7.2. *Viscoelastic properties of liver tissue and constitutive modeling*

The fact that there is considerable difference in stress response to loading and unloading implies that the history of strain affects the stress, and hence, liver tissue is a viscoelastic material. As first approximation, the viscoelastic properties are assumed to be negligible. This assumption is supported by the observation that the liver tissue is relatively strain rate independent. The contribution of linear viscoelasticity is small relative to overall mechanical properties, particularly for computer aided surgical simulation when the strain rate has less variation and is only moderate quantitatively. Nevertheless, by incorporating the viscoelastic properties of liver tissue into the study will inevitably improve the proposed model.

From our experiments, the average relaxation times for constant strain and stress after compression and elongation are 6.9 s, 51.2 s and 17.5 s, 24.0 s respectively. The corresponding relaxation modulus for compression and elongation are 45.9 N/m and 101.1 N/m respectively with a standard linear solid (or Kelvin model). The resultant stress–strain relationship can barely represent up to 10% of the strain. The study reveals that a linear viscoelastic model is possibly not adequate. Liver is a highly nonlinear viscoelastic material. A nonlinear viscoelastic model which is very computational intensive is required for high accuracy.

The viscoelastic properties and shear forces of soft biological tissue were considered in some recent studies on constitutive equations for liver tissues, e.g. Refs. 68 and 69. There were more studies on viscoelastic properties of brain tissues, e.g. Refs. 70 and 71 since brain tissue is more viscous. Viscoelastic behaviors of liver tissue sample had also been detected in our relaxation and creeping tests, and were reported in Ref. 26. We are in the process of introducing a strain rate dependent component into the combined energy constitutive model. This effort to include the nonlinear viscoelastic effect of liver tissue will be done keeping the computation cost as low as possible so that the model remains feasible for computer aided surgical simulation.

7.3. *Hepatic blood flow and biphasic poroelastic constitutive modeling*

Load testing with an extremely vascular organ such as liver (0.4–1 L of blood, 80% of mass is from cells) under *ex vivo* conditions could produce elastic and viscous behaviors that are different from *in vivo* conditions.[72,73] Liver is very unique in its microanatomy relative to hepatic arterial, portal venous (unique dual input supply) and hepatic venous blood with interconnecting lobular sinusoidal anatomy. Other organs will behave differently when distended with blood under normal vascular pressures.

A living liver is porous, and possibly a biphasic poroelastic model may better represent the experimental data if liver tissues are submerged in circulating Ringer's solution during experiment. To our best knowledge, poroelastic model has not been applied to represent liver's mechanical properties. In addition to its complexity, the poroelastic model has its limitation in biological application — unlike engineering materials such as porous rock, the fluid flow through tiny vessels in the case of liver tissue. These micro-vessels known as capillaries have tangible walls that have different mechanical properties compared to that of liver tissue comprising mainly liver cells. Furthermore, the vascular system is a closed system. Blood perfusing tissue produces an internal pressure or tension that is different from that produced by just perfusing the tissue and letting the perfusate exit through exposed and open vessels as will always be the case when biopsy like samples are tested. In order to approach what occurs in the living body, experiments on a whole intact liver will have to be conducted. Nevertheless, the boundary conditions will be extensive and meaningful data analysis may not be possible.

7.4. *Biomechanics of hepatic vessel*

An alternative will be to separately consider the biomechanics of liver tissue and the vessels in which the blood flow. Modeling of the extensive micro-vessels that flow out from the primary hepatic vascular network is the next step for vascular network modeling. To handle the small sizes and highly irregular shapes of these vessels, statistically geometrical modeling technique is possibly a good approach compared to conventional techniques.

In Conclusion, much work has been accomplished and yet much work remains to be done. Computer aided surgery is a young field — this term originated in the

early 1980s. In recent years, scientists and engineers have paid much attention to applying the physical principles and engineering methods to the behavior of parts of human body, considering it as both a structure and a machine, particularly in computer aided surgical simulation. However, it soon become apparent that what have be taken for granted in conventional engineering no longer necessarily applies.

The passive material properties of biological tissues are not linearly elastic. As is shown here, the liver tissue is non-homogeneous, possibly incompressible, highly nonlinear, largely nonlinear viscoelastic and transversely isotropic. The liver tissue is rather porous and the interstitium is filled with fluid. When all of these factors are coupled, the problem of how to describe the mechanical properties of liver tissue in a simple and accurate mathematical form for computer aided surgery becomes quite acute. Furthermore, as a living organism, liver tissue responses to stress and strain biologically as well as mechanically. The complexity of modeling will increase when considering diseased organs where the technology will find most useful application. Surgeons do not operate on normal organs so future work needs to consider how conditions such as cirrhosis/fibrosis, inflammation, infection or lesions such as tumors or cysts need to be eventually incorporated into the biomechanical modeling process. This is a difficult task and will require diseased human fresh autopsy or experimental animal tissue samples. It is only natural to start on normal tissue, but eventually, disease processes need to be considered, especially when considering the interactions of instruments and the tissue.

Knowledge of anatomy and physiology is as important as the engineering principles in biomechanics. The various constitutive equations described here, with hypothesis ranging from linear elastic, hyperelastic, multi-linear, viscoelastic to porous materials, represent only a modest effort in this challenging field. The various sophisticated approaches in biomechanics for engineering analysis may not be done at interactive speeds demanded by typical computer aided surgical application, but it is often desirable to interact with the simulation as it happens to steer the computation so as to improve treatment outcomes. Advancement in computational techniques coupled with the advancement in computing hardware may remedy the often conflicting requirement of accuracy and interactivity. This will contribute to the further integration of biomechanics with computer simulation in computer aided surgery.

Acknowledgments

This work is partially supported by "Research for the Future Program (JSPS-RFTF 99I00904)" funded by Japan Society for the Promotion of Science and "Research on medical devices for analyzing, supporting and substituting the function of human body" funded by Ministry of Health, Labor and Welfare. We would like to acknowledge the following individuals in University of Tokyo for their contributions to this ongoing scientific endeavor: Dr. Etsuko Kobayashi, A/Prof. Xien Chen, Prof. Toshiaki Hisada, Mr. Yosuke Nishimura and Mr. Kengo Mayumi. Valuable comments on the drafts from Prof. James H. Anderson, Johns Hopkins University School of Medicine, Dr. Chee-Cheon Chui, Defence Science Organization, Singapore and Prof. Teoh Swee Hin, National University of Singapore, Singapore were appreciated.

References

1. R. B. Metson, M. J. Cosenza and M. J. Cunningham, Physician experience with an optical image guidance system for sinus surgery, *Laryngoscope* 110(6) (1995) 972–976.
2. G. Burdea, *Force and Touch Feedback for Virtual Reality* (Wiley, New York, 1996).
3. P. N. Brett, C. A. Fraser, M. Henningan, M. V. Griffiths and Y. Kamel, Automated surgical tools for penetrating flexible tissue, *IEEE Eng. Med. Biol.* (1997) 264–270.
4. J. M. Rolfe and K. J. Staples, *Flight Simulators* (Cambridge University Press, England, 1986), pp. 232–249.
5. J. Wachtel, The future of nuclear plant simulation in the United States, in *Simulation for Nuclear Reactor Technology*, D. G. Walton, ed. (Cambridge University Press, England, 1985), p. 339–349.
6. J. H. Anderson, C. Chui, Y. Cai, Y. Wang, Z. Li, X. Ma, W. L. Nowinski, M. Solaiyappan, K. Murphy, P. Gailloud and A. Venbrux, Virtual reality training in interventional radiology — the Johns Hopkins and Kent Ridge Digital Laboratory experience, *Semin. Interven. Radiol.* 19(2) (2002), 179–185.
7. C. Chui, J. H. Anderson and W. L. Nowinski, A simulation system to design and evaluate patient-specific interventional radiology medical devices, in *Business Briefing: Medical Device Manufacturing and Technology* (World Markets Research Centre, United Kingdom, 2002).
8. Y. Cai, C. Chui, X. Ye, J. H. Anderson, K. M. Liew and I. Sakuma, Simulation-based virtual prototyping of customized catheterization devices, *ASME J. Comput. Inform. Sci. Eng.* 4 (2004) 132–139.
9. K. Miller and K. Chinzei, Modeling of soft tissues deformation, *J. Comput. Aided Surg.* 1(Suppl.) (1995) 62–63.
10. I. Sakuma, T. Awao, K. Masamune, T. Nakagori, T. Asano, H. Inada and T. Dohi, Passive navigation system for precise positioning of a needle electrode in radio frequency ablation, *Proc. Comput. Assisted Radiol. Surg.* (2000), p. 978.
11. D. Sorid and S. K. Moore, The virtual surgeon, *IEEE Spectrum* (2000), pp. 26–31.
12. D. L. G. Hill, C. R. Maurer, R. J. Maciunas, J. A. Barwise, J. M. Fitzpatrick and M. Y. Wang, Measurement of intraoperative brain surface deformation under a craniotomy, *Neurosurgery* 43(2) (1998) 514–526.
13. F. J. Carter, T. G. Frank, P. J. Davies, D. McLean and A. Cuschieri, Biomechanical testing of intra-abdominal soft tissue, *Med. Image Anal.* 5 (2001) 231–236.
14. R. Muthupillai, D. J. Lomas, P. J. Rossman, J. F. Greenleaf, A. Manduca and R. L. Ehman, Magnetic resonance elastography by direct visualization of propagating acoustic strain waves, *Science* 269(99) (1995) 1854–1857.
15. A. P. Pathak, M. B. Silver-Thorn, C. A. Thierfelder and T. E. Prieto, A rate-controlled indentor for *in vivo* analysis of residual limb tissues, *IEEE Trans. Rehabilitation Eng.* 6(1) (1998) 12–20.
16. S. K. Kyriacou, C. Schwab and J. D. Humphrey, Finite element analysis of nonlinear orthotropic hyperelastic membranes, *Comput. Mech.* 18 (1996) 269–278.

17. M. Kauer, V. Vuskovic, J. Dual, G. Szekely and M. Bajka, Inverse finite element characterization of soft tissue, *Proc. MICCAI 2001, LNCS 2208* (Springer–Verlag, New York, 2001), pp. 128–136.
18. P. J. Davies, F. J. Carter and A. Cuschieri, Mathematical modelling for keyhole surgery simulation: A biomechanical model for spleen tissue, *IMA J. Appl. Math.* 67 (2002) 41–67.
19. H. Tie and J. P. Desai, A biomechanical model of the liver for reality-based haptic feedback, *MICCAI(1) 2003, LNCS 2878* (Springer–Verlag, New York, 2003), pp. 75–82.
20. K. Onodera, X. Chen, T. Hisada, Identification of biomechanical material properties of soft tissues, *Proc. Jpn. Comput. Eng. Soc. Ann. Conf.* 2001 (Tokyo, Japan, 2001), (in Japanese).
21. J. Kim and M. A. Srinivasan, Characterization of viscoelastic soft tissue properties from *In vivo* animal experiments and inverse FE parameter estimation, in *Proceedings MICCAI 2005, LNCS 3750*, J. Duncan and G. Gerig, eds. (Springer–Verlag, New York, 2005), pp. 599–606.
22. Y. Fung, *Biomechanics — Mechanical Properties of Living Tissues*, Second Edition (Springer–Verlag, New York, 1993).
23. H. Yamada, *Strength of Biological Materials* (Williams & Wilkins, Baltimore, USA, 1970).
24. K. Miller and K. Chinzei, Constitutive modelling of brain tissue: Experiment and theory, *J. Biomech.* 30(11/12) (1997) 1115–1121.
25. C. Chui, E. Kobayashi, X. Chen, T. Hisada and I. Sakuma, Combined compression and elongation experiments and nonlinear constitutive modeling of liver tissue for surgical simulation, *IFMBE J. Med. Biolog. Eng. Comput.* 42(6) (2004) 787–798.
26. I. Sakuma, Y. Nishimura, C. Chui, E. Kobayashi, H. Inada, X. Chen and T. Hisada, *In vitro* measurement of mechanical properties of liver tissue under compression and elongation using a new test piece holding method with surgical glue, in *Surgical Simulation and Soft Tissue Modeling, LNCS 2673*, N. Ayache and H. Delingette, eds. (Springer–Verlag, New York, 2003), pp. 284–292.
27. K. Hayashi, N. Stergiopulos, J.-J. Meister, S. E. Greenwald and A. Rachev, Techniques in the determination of the mechanical properties and constitutive laws of arterial walls, in *Cardiovascular Techniques*, C. Leondes, ed. (CRC Press, 2001), Chapter 6.
28. C. Bruyns and M. Ottensmeyer, Measuring soft-tissue mechanical properties to support development of a physically based virtual animal model, in *MICCAI 2002, LNCS 2488*, T. Dohi and R. Kikinis, eds. (Springer–Verlag, New York, 2002), pp. 283–289.
29. G. J. Tortora, *Principles of Human Anatomy*, 9th Edition (John Wiley & Sons, 2002).
30. D. Haemmerich, I. dos Santos, D. J. Schutt, J. G. Webster and D. M. Mahvi, *In vitro* measurements of temperature-dependent specific heat of liver tissue, *Med. Eng. Phys.* 28(2) (2006) 194–197.
31. K. J. Chua, S. K. Chou and J. C. Ho, An analytical study on the thermal effects of cryosurgery on selective cell destruction, *J. Biomech.* 40(1) (2006) 100–116.
32. C. Chui, Y. Nishimura, E. Kobayashi, H. Inada and I. Sakuma, A medical simulation system with unified multilevel biomechanical model, *Proc. 5th Asian Pacific Cong. Med. Biolog. Eng.* 2002 (CDROM).
33. J. Vossoughi, Constitutive modelling of biological materials, in *The Biomedical Engineering Handbook*, J. D. Bronzino, ed. (CRC Press, 1995), pp. 263–272.

34. P. J. Davies, F. J. Carter, D. G. Roxburgh and A. Cuschieri, Mathematical modelling for keyhole surgery simulations: Spleen capsule as an elastic membrane, *J. Theoret. Med.* 1 (1999) 247–262.
35. K. Miller, Constitutive modelling of abdominal organs, *J. Biomech.* 33 (2000) 367–373.
36. J. W. Melvin, R. L. Stalnaker and V. L. Roberts, Impact injury mechanisms in abdominal organs, *SAE Trans.* 730968 (1973) 115–126.
37. T. T. Tanaka and Y. C. Fung, Elastic and inelastic properties of the canine aorta and their variation along the aortic tree, *J. Biomech.* 7(4) (1974) 357–370.
38. Y. Fung, Elasticity of soft tissues in simple elongation, *Am. J. Physiol.* 213 (1967) 1532–1544.
39. R. M. Kenedi, T. Gibson and C. H. Daly, Bioengineering studies of human skin: the effects of unidirectional tension, in *Structure and Function of Connective and Skeletal Tissue*, S. F. Jackson, S. M. Harkness and G. R. Tristram, eds. (Scientific Committee, St. Andrews, Scotland, 1964), pp. 388–395.
40. M. D. Ridge and V. Wright, The description of skin stiffness, *Biorheology* 2 (1964) 67–74.
41. F. R. Schmidlin, M. Thomason, D. Oller, W. Meredith, J. Moylan, T. Clancy, P. Cunningham and C. Baker, Force transmission and stress distribution in a computer simulated model of the kidney: An analysis of the injury mechanisms in renal trauma, *J. Trauma* 40 (1996) 791–796.
42. M. Farshad, M. Barbezat, F. Schmidlin, L. Bidaut, P. Niederer and P. Graber, Material characterization and mathematical modeling of the pig kidney in relation with biomechanical analysis of renal trauma, *Proc. North Am. Cong. Biomech.* (Waterloo, Ontario, Canada, 1998).
43. M. Mooney, A theory of large elastic deformation, *J. Appl. Phys.* 11 (1940) 582–592.
44. D. R. Veronda and R. A. Westmann, Mechanical characterizations of skin-finite deformations, *J. Biomech.* 3(1) (1970) 111–124.
45. K. Takamizawa and K. Hayashi, Strain energy density function and uniform strain hypothesis for arterial mechanics, *J. Biomech.* 20(1) (1987) 7–17.
46. K. Hayashi, Experimental approaches on measuring the mechanical properties and constitutive laws of arterial walls, *ASME J. Biomech. Eng.* 115 (1993) 481–487.
47. J. Xie, J. Zhou and Y. Fung, Bending of blood vessel wall: Stress-strain laws of the intima-media and adventitial layers, *ASME J. Biomech. Eng.* 117 (1995) 136–145.
48. T. Hisada and H. Noguchi, *Principle and Application of Non Linear Finite Element Methods* (Maruzen, Tokyo, Japan, 1995) (in Japanese).
49. M. E. Zobitz, Z. Luo and K. An, Determination of the compressive material properties of the supraspinatus tendon, *ASME J. Biomech. Eng.* 123 (2001) 47–51.
50. D. Bogen, Strain energy description of biological swelling I single fluid compartment models, *ASME J. Biomech. Eng.* 109 (1987) 252–256.
51. Y. Fung, S. Liu and J. Zhou, Remodeling of the constitutive equation while a blood vessel remodels itself under stress, *ASME J. Biomech. Eng.* 115 (1993) 453–459.
52. Y. Fung, Biorheology of soft tissue, *Biorheology* 10 (1973) 139–155.
53. Y. Ling, Uniaxial true stress-strain after necking, *AMP J. Technol.* 5 (1996) 37–48.
54. H. Demiray, A note of the elasticity of soft biological tissues, *J. Biomech.* 5(3) (1972) 309–311.
55. D. Terzopoulos and K. Fleischer, Deformable models, *The Visual Comput.* 4 (1988) 306–331.
56. S. Cotin, H. Delingette and N. Ayache, Real-time volumetric deformable models for surgical simulation using finite elements and condensation, in *Proc. Eurograph. 96* (Springer–Verlag, New York, 1996), pp. 57–66.

57. G. Szekely, C. Brechbuehler, R. Hutter, A. Rhomberg, N. Ironmonger and P. Schmid, Modeling of soft tissue deformation for laparoscopic surgery simulation, *Med. Image Anal.* 4 (2000) 57–66.
58. S. K. Kyriacou and D. Davatzikos, A biomechanical model of soft tissue deformation with applications to non-rigid registration of brain images with tumor pathology, in *Proc. MICCAI 98, LNCS 1496* (Springer–Verlag, New York, 1998), pp. 531–538.
59. J. B. A. Mains and M. A. Viergever, A surgery of medical image registration, *Med. Image Analy.* 2(1) (1998) 1–36.
60. D. J. Hawks, P. J. Ewards, D. Barratt, J. M. Blackall, G. P. Penney and C. Tanner, Measuring and modeling soft tissue deformation for image guided interventions, in *Surgical Simulation and Soft Tissue Modeling, LNCS 2673*, N. Ayache and H. Delingette, eds. (Springer–Verlag, New York, 2003), pp. 1–14.
61. H. F. Reinhart, CT-guided real-time stereotaxy, *Acta Neurochir. Suppl.* 46 (1989) 107–108.
62. D. Aulignac, R. Balaniuk and C. Laugier, A haptic interface for a virtual exam of the human thigh, *Proc. IEEE Int. Conf. Robotics Automat.* (2000), pp. 2452–2456.
63. I. Brouwer, Measuring *in vivo* animal soft tissue properties for haptic modeling in surgical simulation, in *Proc. Med. Meets Virtual Reality* (IOS Press, 2001), pp. 69–74.
64. S. Doko, J. J. LeGrice and B. H. Smaill, A triaxial-measurement shear-test device for soft biological tissues, *J. Biomech. Eng.* 122 (2000) 471–478.
65. A. E. Kerdok, Soft tissue characterization: mechanical property determination from biopsies to whole organs, *Whitaker Foundation Biomedical Research Conference*, 2001.
66. J. G. Snedeker, M. Barbezat, P. Niederer, F. R. Schmidlin and M. Farshad, Strain energy as a rupture criterion for the kidney: Impact tests on porcine organs, finite element simulation, and a baseline comparison between human and porcine tissues, *J. Biomech.* 38 (2005) 993–1001.
67. D. L. Vawter, Y. C. Fung and J. B. West, Constitutive equation of lung tissue elasticity, *ASME J. Biomech. Eng.* 101 (1980) 38–45.
68. Z. Liu and L. Bilston, On the viscoelastic character of liver tissue: Experiments and modeling of linear behavior, *Biorheology* 37(3) (2002) 191–201.
69. Z. Liu and L. Bilston, Large deformation shear properties of liver tissue, *Biorheology* 39(6) (2000) 735–742.
70. D. W. A. Brands, G. W. M. Peters and P. H. M. Bovendeerd, Design and numerical implementation of a 3D nonlinear viscoelastic constitutive model for brain tissue during impact, *J. Biomech.* 37 (2004) 127–134.
71. L. Bilson, Z. Liu and N. Phan-Tien, Large strain behavior of brain tissue in shear — Some experimental data and differential constitutive model, *Biorheology* 38 (2001) 335–345.
72. J. D. Brown, J. Rosen, Y. S. Kim, L. Chang, M. N. Sinanan and B. Hannaford, *In vivo* and *in situ* compressive properties of porcine abdominal soft tissues, in *Proc. Med. Meets Virtual Reality* (IOS Press, 2003), pp. 26–32.
73. A. E. Kerdok, M. P. Ottensmeyer and R. D. Howe, The effects of perfusion on the viscoelastic characteristics of liver, *J. Biomech.* (2005) In Press.
74. C. Chui, E. Kobayashi, X. Chen, T. Hisada and I. Sakuma, Tranversely isotropic properties of porcine liver tissue: Experiments and constitutive modeling, *Med. Biol. Eng. Comput.* 45(1) (2007) 99–106.

CHAPTER 8

ULTRASOUND MEASUREMENT OF SWELLING BEHAVIORS OF ARTICULAR CARTILAGE *IN SITU*

QING WANG and YONG-PING ZHENG*
Department of Health Technology and Informatics
The Hong Kong Polytechnic University
Kowloon, Hong Kong, China
**ypzheng@ieee.org*

1. Introduction

1.1. *Articular cartilage*

Articular cartilage is the thin white layer of soft connective tissue that covers the articulating bony ends in diarthrodial joints, such as the end surfaces of the tibia and femur, and the posterior surface of the patella inside the knee joint. Although articular cartilage is a tiny tissue in the body, it provides joints with excellent lubrication and wearing characteristics, and maintains a smooth efficient force-bearing system. It is hard to imagine how the skeleton to bear the weight of the body and conduct the movement without articular cartilage. It has been found that the exact compositions and structure of articular cartilage depend greatly on anatomy location, depth, and age, as well as the pathological state of the tissue.[1–3] The complex hydrated-charged nature and magic functions of articular cartilage have attracted tremendous research interests.

1.1.1. *Negative charged proteoglycan-collagen matrix*

Chondrocytes, proteoglycans (PGs), collagens and water are the major components of articular cartilage. Therefore, articular cartilage is usually regarded to consist of chondrocytes and extracellular matrix (ECM, 95% of the total wet weight).[1] The ECM is primarily composed of water (75% of wet weight), collagen fibrils (mainly type II) (20%), PGs (5%), and other components, such as enzymes, growth factors, lipids, and adhesives.[1]

PGs and collagens interact with each other to form the porous solid matrix swollen with water. PGs are bio-macromolecules, produced by chondrocytes and secreted into the matrix. A single PG aggregan molecule consists of a protein core to which numerous glycosaminoglycan (GAG) chains are bounded by sugar bonds. The aggregated PGs are strongly electronegative due to the negatively charged groups

解説

V．肺癌の発見と診断

4. 肺癌の画像診断—内視鏡所見

土田敬明（国立がんセンター中央病院内視鏡部）

●Key Words
lung cancer, bronchoscopy, diagnosis

はじめに

evidence-based medicine（EBM）の手法による肺癌の診療ガイドライン策定に関する研究班によれば，気管支鏡は，肺癌が疑われる中枢気管支病変に対して施行するよう強く勧められている[1]．したがって，肺癌が疑われる中枢気管支病変に対して気管支鏡検査がなされることになるが，その所見の取り方，所見の記載に関しては，見逃しや誤診を極力少なくするためにも標準化が必要である．肺癌における中枢気管支の内視鏡所見分類は日本肺癌学会による肺癌取扱い規約[1]に記載のものが広く用いられている．本稿では，肺癌を疑う気管支鏡所見について，肺癌取扱い規約の分類に基づいて概説する．

Ⅰ．非早期肺癌の内視鏡所見

肺癌取扱い規約によると，非早期肺癌の内視鏡所見は腫瘍の増殖形態により分類されている．すなわち，1）粘膜型（上皮層および上皮下層を破壊して増殖），2）粘膜下型（粘膜下に浸潤増殖），および3）壁外型（壁外に増殖）に大きく分類される．さらに，1）粘膜型はa）肥厚型，b）結節型，およびc）ポリープ型に分類される．それぞれの細かい気管支鏡所見は，腫瘍そのものによる「直接所見」と腫瘍による2次変化と考えられる「間接所見」に区別され，さらにそれぞれの所見として，a. 凹凸不整，b. 血管の怒張，c. 壊死・白苔，d. 潰瘍，e. 発赤，f. 出血，g. 狭窄，h. 閉塞，i. 粘膜襞の肥厚，消失，j. 腫脹（浮腫），k. 軟骨輪の不鮮明化，l. 分岐の開大，鈍化があげられている．

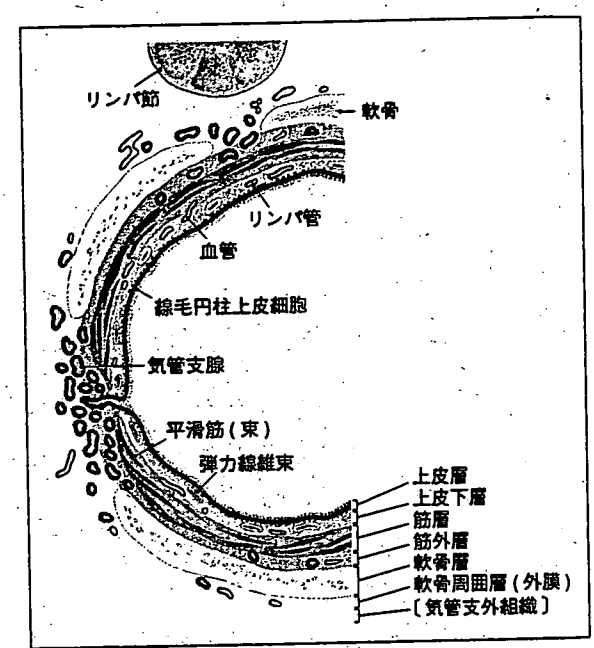

【図1】気管支壁の層構造（文献1）より引用改変）

1．粘膜型

a. 肥厚型

図3に肥厚型の非早期癌を呈示する．図3aでは，凹凸不整，壊死，狭窄，閉塞，粘膜襞の肥厚および消失，腫脹，軟骨輪の不鮮明化，分岐の開大が認められる．癌，特に扁平上皮癌を強く疑う所見であるが，炎症においても同様の所見を呈することがあり，生検による確定診断を要する．図3bでは，図3aの所見に加えて発赤が認められる．図3cでは出血を呈しているが壊死は認められず，腺癌による所見との鑑別を要する．図3dは，一部結節様の隆起を呈しているがほぼ平坦で，肥厚型に分類した．微小ではあるが壊死も認められ扁平上皮癌を疑う所見である．図3eは，分岐の開大を呈する肥厚型の非早期肺癌である．壁外型

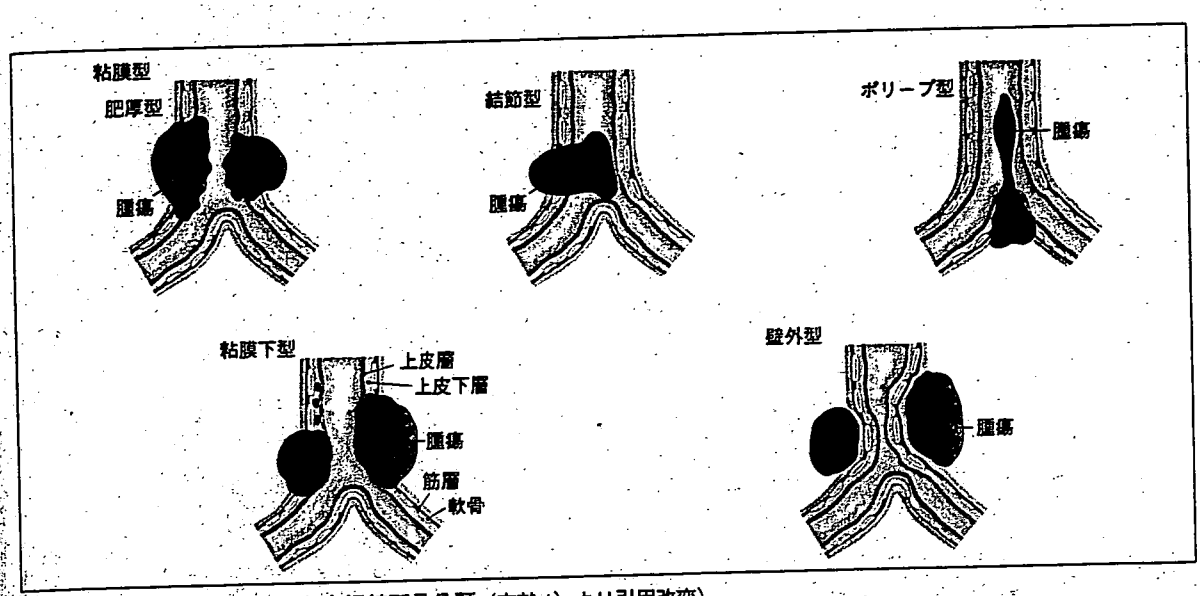

[図2] 腫瘍増殖形態からみた内視鏡所見分類（文献1）より引用改変）

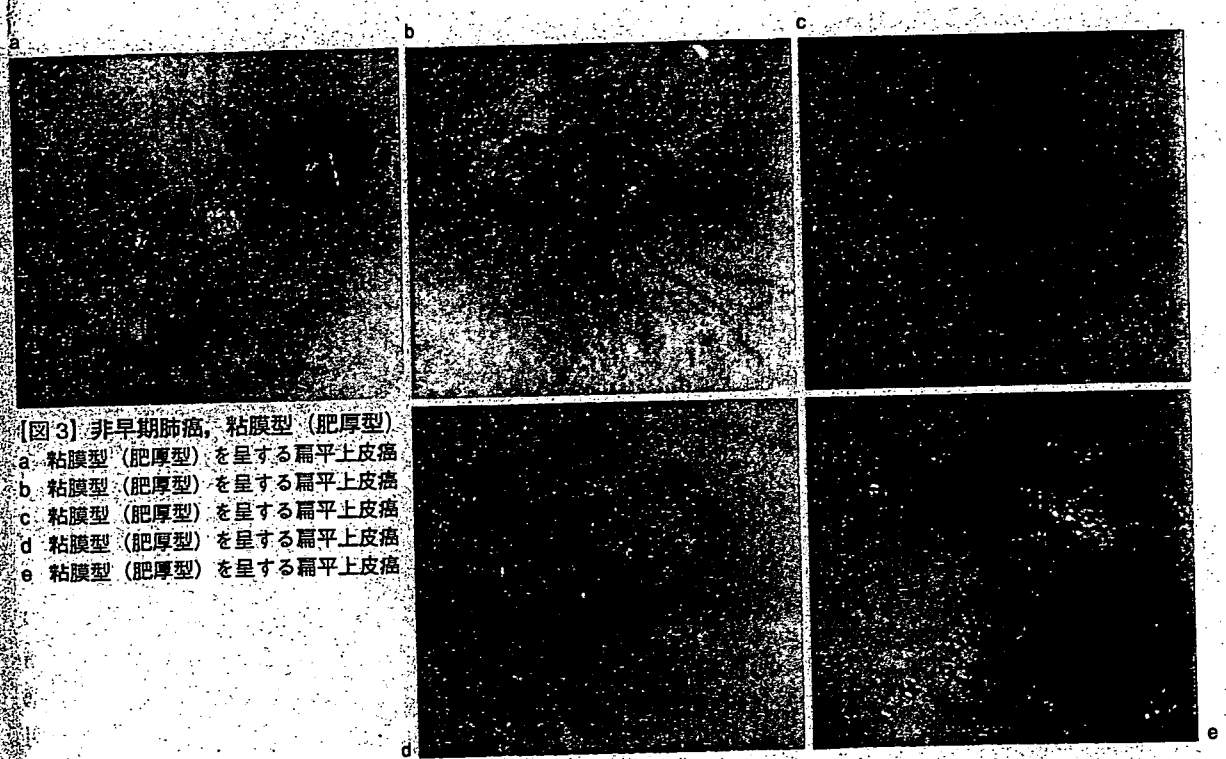

[図3] 非早期肺癌，粘膜型（肥厚型）
a 粘膜型（肥厚型）を呈する扁平上皮癌
b 粘膜型（肥厚型）を呈する扁平上皮癌
c 粘膜型（肥厚型）を呈する扁平上皮癌
d 粘膜型（肥厚型）を呈する扁平上皮癌
e 粘膜型（肥厚型）を呈する扁平上皮癌

の分岐の開大（図7a）との鑑別を要するが，粘膜面が粗糙（直接所見）であることから粘膜型に分類される．また，まれではあるが，良性腫瘍で粘膜型病変に類似した所見を呈するものがある（図8a）．

b. 結節型

図4に結節型の非早期癌を呈示する．直接所見が隆起性かつ広基性病変である場合，結節型として分類される．図4aは結節型を呈する扁平上皮癌である．広基性の隆起で壊死を伴っている．壊死を伴う結節型病変では扁平上皮癌を疑う．図4bも壊死を伴う結節性病変であるが，隆起部分の周囲には粘膜の凹凸不整，粘膜襞の肥厚および消失，腫脹，軟骨輪の不鮮明

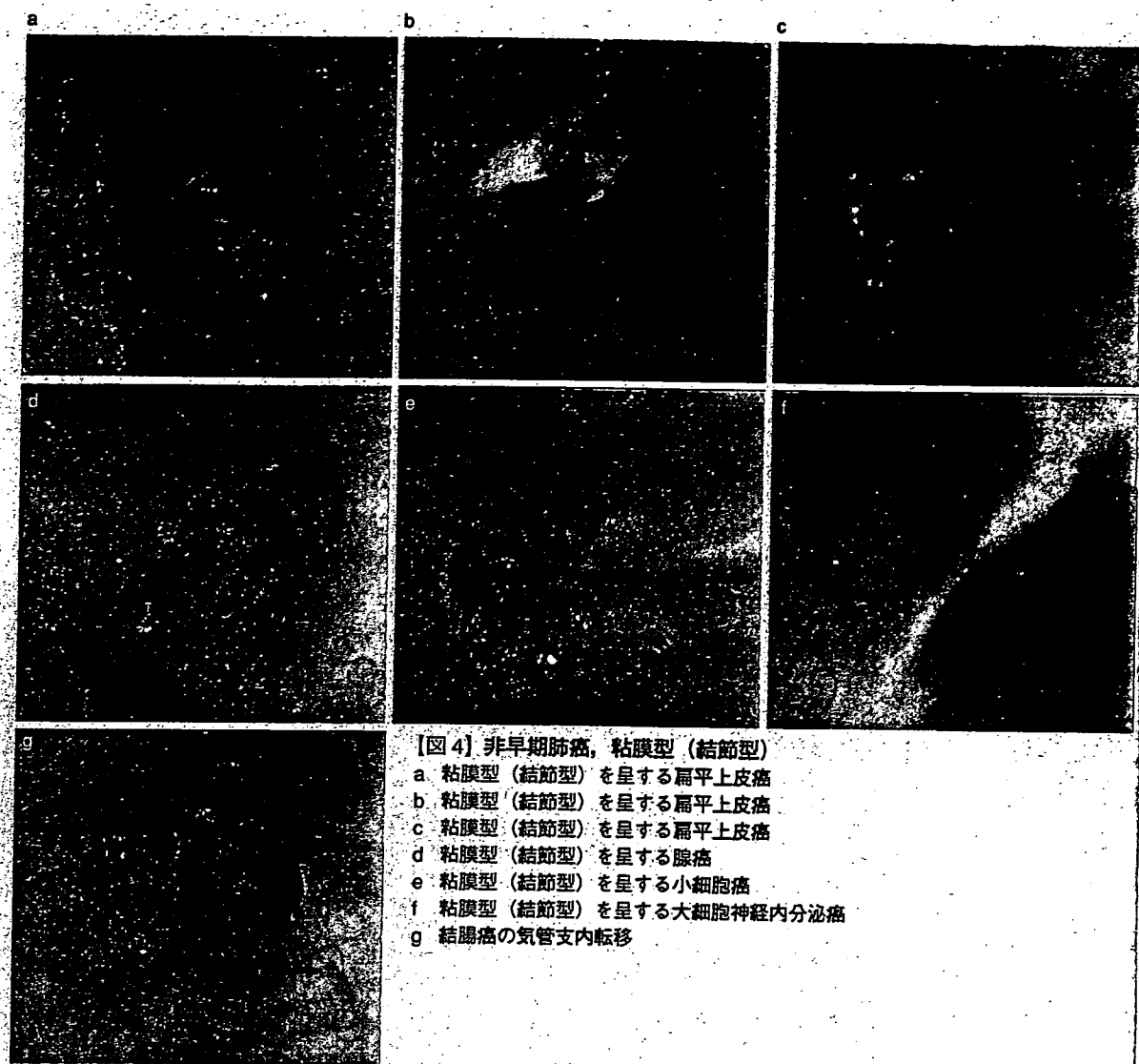

【図4】非早期肺癌，粘膜型（結節型）
a 粘膜型（結節型）を呈する扁平上皮癌
b 粘膜型（結節型）を呈する扁平上皮癌
c 粘膜型（結節型）を呈する扁平上皮癌
d 粘膜型（結節型）を呈する腺癌
e 粘膜型（結節型）を呈する小細胞癌
f 粘膜型（結節型）を呈する大細胞神経内分泌癌
g 結腸癌の気管支内転移

化などの間接所見が認められ，周囲への進展が疑われる．図4cは壊死を伴わない結節型の病変である．本例は生検により扁平上皮癌が確認されたが，他部位からの気管支内転移（図4g，図5f）や良性病変（図8b，c）との鑑別を要する．肺の腺癌や小細胞癌で結節型の病変を呈するものの多くはリンパ節からの直接進展であり，分岐の開大を伴っていることが多く，病変の主体は粘膜下または壁外であることが鑑別点となる．図4dは腺癌における結節型病変である．病変の主体は粘膜下あるいは壁外であり，結節型の病変はリンパ節からの進展によるものと考えられる．図4eは小細胞癌における結節型病変である．この病変も主体は粘膜下である．小細胞癌では間接所見として血管の怒張を伴うことが多い．図4fは大細胞神経内分泌癌における結節型病変である．内視鏡的には粘膜下や壁外の病変による所見は明らかではないが，CTでは明らかなリンパ節の腫脹を認めており，リンパ節からの進展が考えられた．このような症例では，CT所見を参考にした病変の解釈が必要である．他臓器からの転移でも結節型の病変を呈する場合がある．図4gは結腸癌の気管支内転移である．壊死を伴わない粘膜主体の結節性病変の場合，他臓器からの転移を念頭におく必要がある．このような転移は気管支動脈を介している場合があり，生検により大出血を起こす可能性を秘

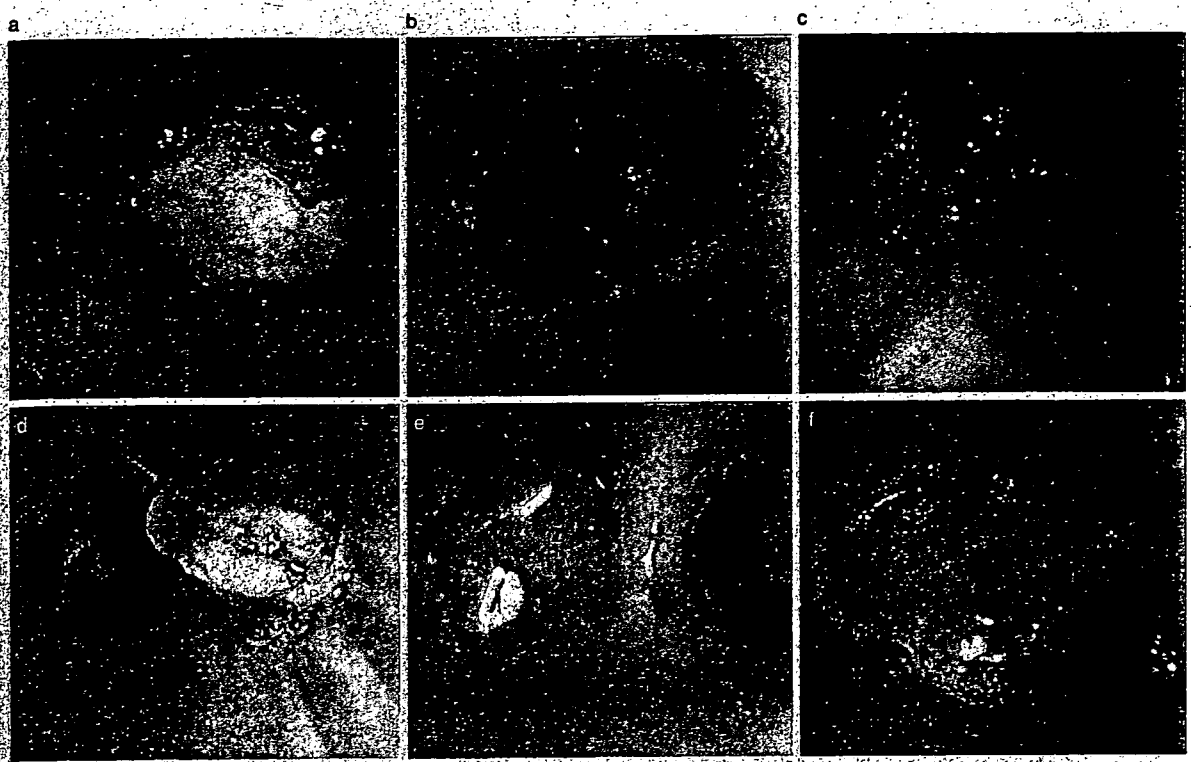

【図5】非早期肺癌，粘膜型（ポリープ型）
a 粘膜型（ポリープ型）を呈する扁平上皮癌
b 粘膜型（ポリープ型）を呈する扁平上皮癌
c 粘膜型（ポリープ型）を呈する扁平上皮癌
d 粘膜型（ポリープ型）を呈する腺癌
e 粘膜型（ポリープ型）を呈する腺癌
f 乳癌の気管支内転移

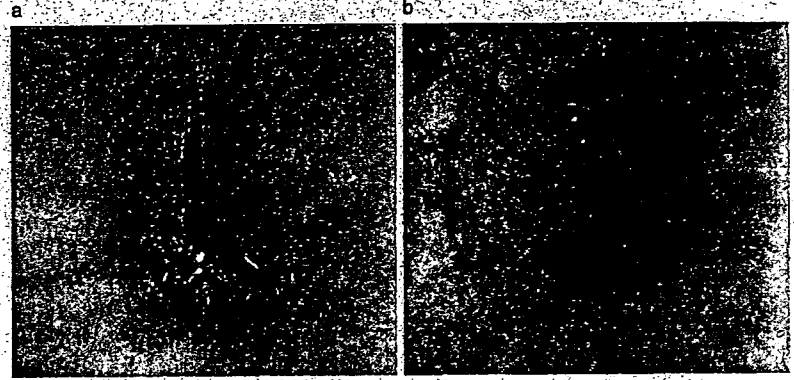

【図6】非早期肺癌，粘膜下型
a 粘膜下型を呈する腺癌
b 粘膜下型を呈する小細胞癌

めている．この場合，病変が小さいほど要注意となる．

c．ポリープ型

図5にポリープ型の非早期癌を呈示する．直接所見が隆起型でかつ有茎性の場合ポリープ型と分類される．図5aでは腫瘤は壊死物質で覆われており，扁平上皮癌を疑う．図5bは左主気管支の縦隔側に認められたポリープ型の腫瘤である．リンパ節からの進展のようにもみえるが，よく観察すると壊死を伴っており，扁平上皮癌が疑われた．図5cは壊死を伴わない扁平上皮癌である．定型的ではないが，扁平上皮癌でも壊死を伴わないポリープ型を呈することがある．図5dはポリープ型を呈する腺癌である．壊死を伴うようにみえるが，白色のものは吸引にて容易に除去され，喀痰と考えられた．図5eは末梢側より管腔内に突出してきた腺癌である．表面は光沢があり粘膜層は保たれていると考えられる．厳密には粘膜下型とすべきであるが，ポリープ状になっている場合はポリープ型に分類されることが多い．原発性肺癌以外にもポリープ型の腫瘤を形成するものがあり（図5f），結節型と同様注意を要する．

2．粘膜下型

図6に粘膜下型の非早期癌を呈示する．腺癌や小

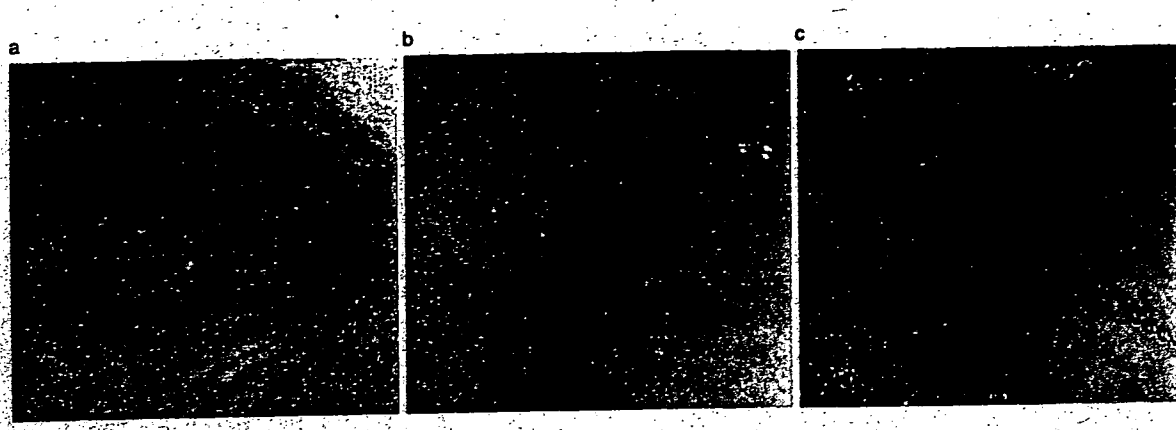

【図7】壁外型
a 壁外型を呈する腺癌
b 壁外型を呈する腺癌
c 壁外型を呈する小細胞癌

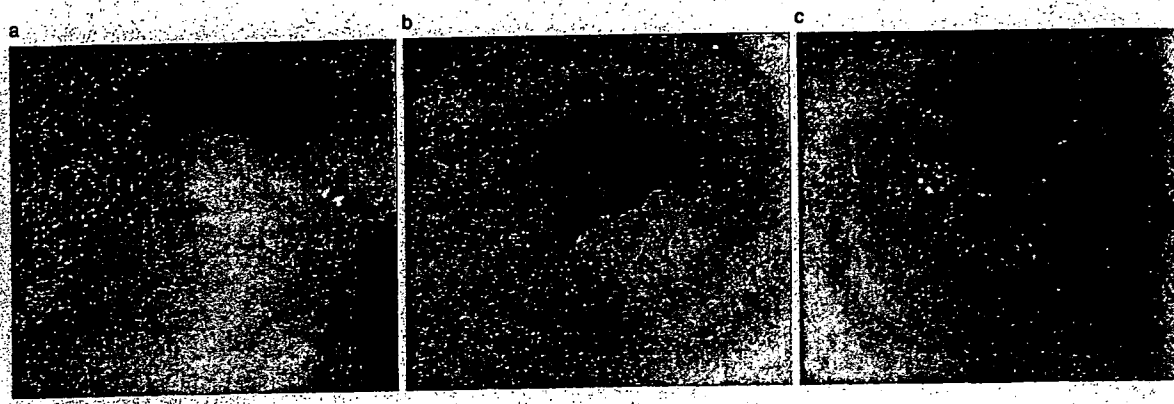

【図8】良性病変
a 気管支顆粒細胞腫
b 気管支脂肪腫
c 気管支腺腫

細胞癌では粘膜下型を呈することが多い（図6a，b）．特に，小細胞癌では血管の怒張が特徴的所見となる（図6b）．

3．壁外型

図7に壁外型の非早期癌を呈示する．図7aでは気管分岐部の開大が認められ，気管分岐部リンパ節への転移が疑われた．図7bでは壁外からの圧排により気道狭窄を呈している．図7cは壁外型を呈する小細胞癌である．粘膜面に血管怒張が観察される．

II．肺門部早期肺癌の内視鏡所見

肺門部早期肺癌の内視鏡所見は，基本型と間接所見により分類されている．基本型としては，1）無所見型，2）肥厚型，3）結節型，4）ポリープ型に分類される（図9）．基本型以外にも次のような間接所見がみられることがある．すなわち，a．病巣の表層の変化として不整，細顆粒状，波打ち状など，b．壊死・

【表1】肺癌取扱い規約による内視鏡的肺門部早期癌の診断基準

基準A：臨床的基準
2．胸部X線写真（断層およびCT像を含む）が正常像であること
3．通常の病期診断に用いられる方法によりリンパ節および遠隔転移がないこと
基準B：内視鏡的基準
1．気管から亜区域支までに限局すること
2．病巣の末梢辺縁が，内視鏡的に可視できること
3．病巣の長径が2cm以下であること
4．組織学的に扁平上皮癌であること

【図 9】早期肺癌の内視鏡所見分類
(文献 1) より引用改変)

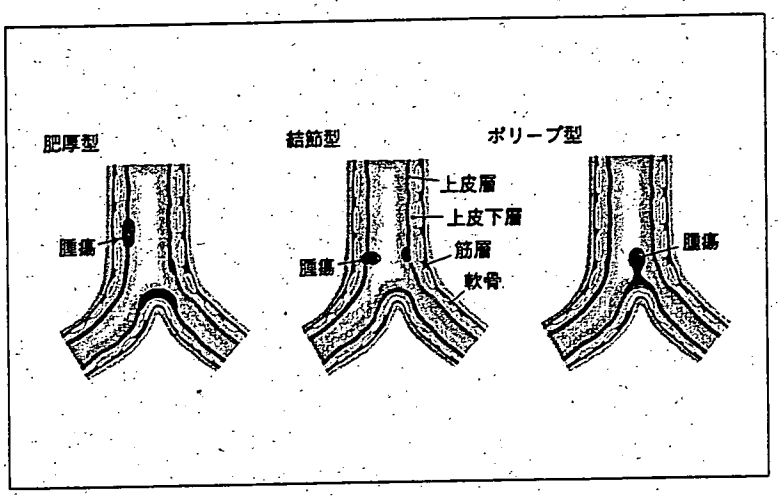

【図 10】早期肺癌，無所見型

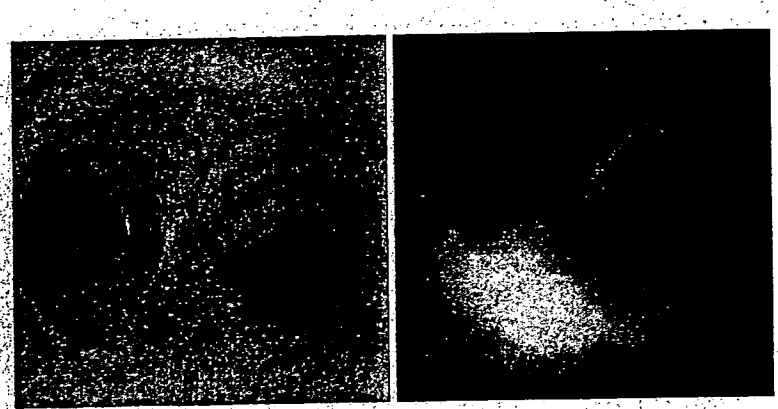

白苔，c. 出血，d. 血管増生・怒張，e. 皺襞の異常，f. 軟骨輪の不明瞭化が間接所見としてまとめられている．これらの所見は，しばしば内視鏡の操作により人為的にできてしまう所見との鑑別がむずかしいものが多く，喀痰細胞診陽性などで気管支鏡検査を行う場合には，なるべく咳をさせない，強い吸引は行わない，スコープを先進させる前に観察を行うなどの配慮が必要である．内視鏡的肺門部早期肺癌の診断基準としては，表 1 に示すとおり，X 線無所見，転移が認められない，病巣の末梢端が内視鏡で観察可能，亜区域支以内に限局，長径が 2cm 以下，組織は扁平上皮癌とされている．ただし，長径の判定は通常の気管支鏡のみでは困難なことが多く，腫瘍進展範囲の判定には蛍光内視鏡を使用することが望ましい．

1．無所見型

この型の早期癌は一般に発見は困難である．喀痰細胞診で陽性または疑陽性で蛍光内視鏡による検査がなされた場合にまれに報告される．図 10 は，喀痰細胞診が陽性で蛍光内視鏡検査を行ったところ気管分岐部に蛍光の欠落部分を認め，同部位の生検により扁平上皮癌の診断を得た．通常の電子内視鏡では病変を指摘し得ないが，光感受性物質（レザフィリン）投与後の蛍光内視鏡では病変部に赤色の蛍光を認める．

2．肥厚型

図 11 に肥厚型の肺門部早期肺癌を呈示する．図 11a，b では，血管の増生・怒張が認められる．図 11c では，皺襞の異常や軟骨輪の不明瞭化が認められる．いずれも粘膜の肥厚を伴っている．図 11d では，粘膜の肥厚とわずかな血管の増生が認められる．この型の早期癌も微妙な所見が多く，人為的な所見を作らないようにして，かつ，詳細な観察が必要である．

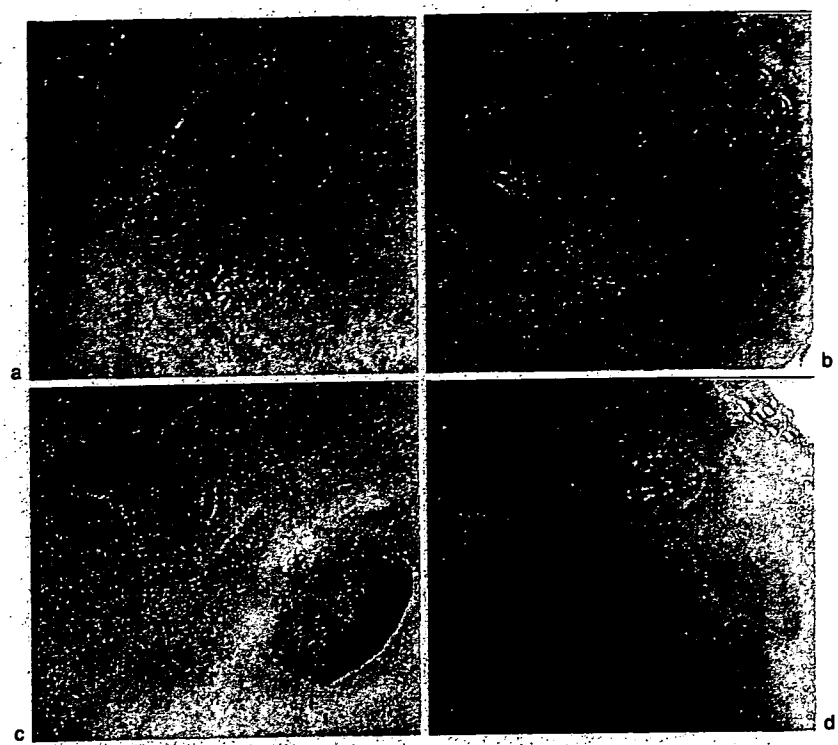

【図11】早期肺癌，肥厚型
a 肥厚型を呈する肺門部早期癌
b 肥厚型を呈する肺門部早期癌
c 肥厚型を呈する肺門部早期癌
d 肥厚型を呈する肺門部早期癌

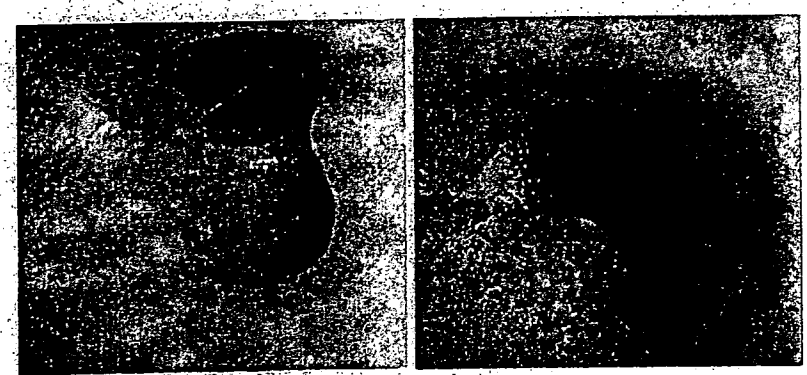

【図12】（左）早期肺癌，結節型
【図13】（右）早期肺癌，ポリープ型

3．結節型

図12に結節型の肺門部早期肺癌を呈示する．表層の不整，壊死，血管増生，皺襞の異常が認められ，病変の存在を指摘することは比較的容易である．

4．ポリープ型

図13にポリープ型の肺門部早期肺癌を呈示する．この型の早期癌は比較的まれである．表面は顆粒状で，赤色点を伴っている．パピローマや気管支内転移，非早期癌などとの鑑別が必要である．

［文献］

1）日本肺癌学会編：肺癌取扱い規約，改訂第6版，金原出版，東京，87-92，2003

2）気管支鏡検査

肺がん患者もしくは肺がんを疑われた患者に対する気管支鏡検査の目的を表2-5に示す．がんの診断目的で気管支鏡検査を行う場合は表に示すように大きく分けて4通りがあるが，この4つの目的の複数を1回の検査で行う場合もある．

表2-5に示された目的は，主に治療前の確定診断あるいは病期（進行度）診断で，表に示した以外にも，化学療法や放射線療法，手術療法の合併症の診断目的や，治療効果の判定目的で気管支鏡検査が行われる場合もある．

a）検査の実際

（1）検査の準備

気管支鏡本体は，検査目的や手技によって種類の異なった内視鏡を用いるため，術者が準備する．多くの場合，細径タイプの電子内視鏡を使用する．また，気管支鏡検査を安全に行うためには，術者（医師），助手（医師），看護師の最低3名が必要である．X線透視下で検査を行うためには，これに加えて放射線技師も必要となる．

（2）本人確認

本人確認は，ネームバンドによる確認が望ましい．口頭で確認する場合は，必ず患者本人にフルネームを名乗ってもらう．

（3）問　診

問診では，検査前禁飲食の確認，当日の体調の確認，抗凝固薬などを使用している場合の休薬の確認，既往歴の確認（アレルギーの有無，緑内障の有無，前立腺肥大の有無など），妊娠可能性の有無，車を運転しないことの確認などを行う．特に車を運転しないことに関しては，本人だけでなく事故になった場合に無関係の第3者を傷つける可能性があることを理解

表2-5●肺がん診断における気管支鏡検査の目的

1．組織診による確定診断，細胞診による悪性診断
　① 中心型（肺門部）肺がんでは，病変を内視鏡で見ながら生検を行う．
　② 末梢型（肺野型）肺がんでは，X線透視下で生検を行う．
2．がんの浸潤範囲の診断
　① がんの広がりを見る場合に，蛍光気管支鏡を用いることもある．
　② がんの深達度の判定のために，超音波気管支鏡を用いることもある．
3．リンパ節転移の有無の診断
　気管または気管支周囲のリンパ節への転移の有無を細胞診または組織診で判定するために，気管または気管支からリンパ節に針を刺して診断材料を採取する．超音波気管支鏡またはCTでリンパ節の位置を把握しながら行う．
4．中心型（肺門部）肺がんの存在診断
　喀痰細胞診で陽性または疑陽性と判定され，CTで病変が指摘されない場合や，1か月以上原因不明の咳が続く場合に，太い気管支にできたがんを疑って行う．蛍光気管支鏡を併用する場合もある．